Nanoscale

Universal Discoidal Nano Platform for Intracellular Delivery of PNAs

Journal:	*Nanoscale*
Manuscript ID	NR-ART-04-2019-003667.R1
Article Type:	Paper
Date Submitted by the Author:	20-May-2019
Complete List of Authors:	Tahmasbi Rad, Armin; University of Connecticut, IMS Malik, Shipra; University of Connecticut Yang, Lin; Brookhaven National Laboratory Oberoi-Khanuja , Tripat Kaur ; University of California San Francisco Nieh, Mu-Ping; University of Connecticut, Chemical and Biomolecular Engineering Bahal, Raman; University of Connecticut

Universal Discoidal Nano Platform for Intracellular Delivery of PNAs

Armin Tahmasbi Rad [a,b,*], Shipra Malik [c,*], Lin Yang [d], Tripat Kaur Oberoi-Khanuja [e], Mu-Ping Nieh [a,b,f,‡], Raman Bahal [c,‡]

[a] Department of Biomedical Engineering, University of Connecticut, Storrs, CT, 06269 USA

[b] Polymer Program, Institute of Materials Sciences, University of Connecticut, 191 Auditorium Road, Storrs, CT 06269, USA

[c] School of Pharmacy, University of Connecticut, Storrs, CT, 06269 USA

[d] National Synchrotron Light Source – II, Brookhaven National Laboratory, Uptone, NY, USA

[e]Department of Dermatology, University of California, San Francisco, CA, USA

[f] Department of Chemical and Bimolecular Engineering, University of Connecticut, Storrs, CT, 06269 USA

[‡] Co-corresponding Author:

Mu-Ping.Nieh@UConn.edu, Raman.Bahal@UConn.edu

[*] These authors contributed equally to this work.

Abstract

Peptide nucleic acids (PNAs) have gained considerable attention due to their remarkable gene editing and targeting based strategies. However, cellular delivery of PNAs always remain a challenge for their broader therapeutic applications. Here, we investigated a novel complex made of lipid bicelles and PNA based carriers for efficient delivery of PNAs. For proof of concept, PNAs targeting microRNA (miR)-210 and 155 have been tested. Comprehensive evaluation of positive as well as negative charge containing bicelles with different PNA:lipid ratios of 1:100, 1:1000 and 1:2500 were performed. The negatively charged bicelles with a PNA:lipid molar ratio of 1:2500 yields a discoidal shape with a uniform diameter of size ~30 nm and a bilayer thickness of 5 nm, while the positively charged bicellar system contains irregular vesicles after incorporation of PNA. Small-angle X-ray scattering (SAXS) analysis was performed to provide the insight into how hydrophobic PNAs interacted with bicelles. Further, flow cytometry followed by confocal microscopy analyses substantiate superior transfection efficiency of bicelles containing dye conjugated antimiR PNAs. Functional analysis also confirmed the miR inhibition by PNA oligomers delivered by bicelles. The nanodiscoidal complex opens a new pathway to deliver PNAs, which are of great challenge to be endocytosed on their own, into cells.

Keywords

Peptide nucleic acids, Nanodisc, MicroRNA, AntimiR

INTRODUCTION

Peptide nucleic acids (PNAs) have expanded widely from last few years not only for their role in basic research but also in therapeutic areas pertaining to gene editing and targeting. PNAs are artificial DNA mimics that consist of pyrimidine or purine nucleobases attached to a highly flexible pseudopeptide backbone[1,2]. It has been well established that PNAs bind with high affinity to genomic DNA and RNA targets based on Watson Crick recognition principles and regulate gene expression[3]. In addition, the neutral backbone of PNAs confers it resistance to enzymatic degradation[4]. The aforementioned unique properties of PNAs make it attractive reagent for therapeutic and diagnostic applications. However, intracellular delivery; how to get PNAs across the lipid bilayers cell membrane, always possess an enormous challenge and circumvent their broader applications[5].

Several promising chemical, mechanical and electrical transduction based methods are explored for increasing intracellular delivery PNAs[6-8]. However, these methods can only apply to small experimental condition and cannot translate to *in vivo* studies as well as for clinical applications. Additionally, transduction reagents often lead to off-target and cytotoxic effects. Similarly, a series of cationic residues conjugated PNAs have been explored that could aid cellular uptake of PNAs by increasing their degree of interaction with negatively charge cell membrane[9]. Though these strategies have shown promise up to a certain extent, however, the inclusion of cationic groups also increases cytotoxicity both *in vitro* as well as *in vivo*. Other possibilities of incorporating the transduction domain onto the achiral backbone of PNAs have been investigated. These include the development of guanidinium and lysine based chemically modified gamma PNAs[10,11]. However, these methods require complicated synthetic procedures and elaborate optimization to generate ample material especially for *in vivo* studies.

Recently, nanoparticles (NPs) based strategies have garnered attention to delivery PNAs for fundamental as well as biomedical research. Several NPs; avidin[12], Zeolites[13],

mesoporous silica[14], and Cationic shell cross-linked knedel-like NPs[15], just to name a few have been reported to deliver PNAs. Moreover, FDA approved poly-lactic-co-glycolic acid (PLGA) based NPs to deliver PNAs has also been tested extensively[6,16,17]. Though these PLGA based NPs has shown promise to some extent, however, it does not yield NPs containing highly payload of PNAs that is necessary for clinical efficacy.

Recently low-polydispersity, spontaneously-forming discoidal bicelle or nanodisc (ND) with a diameter of ~30 nm and a thickness of 5 nm in a mixture of long- and short- chain lipids has been employed for entrapping hydrophobic molecules with a robust formation/assembly mechanism[18,19]. The membrane-mimicking bicelles can be stabilized by polyethyleneglycol conjugated (PEGylated) lipids and easily incorporated with amphiphilic biomolecules such as membrane proteins making them an attractive system for solubilization, isolation, purification, and biophysical and biochemical studies of membrane proteins[20,21]. Our prior study indicated that the cellular uptake of bicelles is ~ 5-10 times more than spherical vesicles with an identical chemical composition, because they take more routes of internalization than the vesicles do [22,23]. Enhanced uptake, more diverse mechanisms for endocytosis and faster diffusion across the membrance due to the small size[24] make bicelles a better candidate than the conventional polymeric and inorganic spherical nanocarriers[25-28,29].

In this study, several bicelles/PNA nanocomplexes were characterized in structure and designed for optimal endocytotic delivery. The new class of nanocarrier shows excellent transfection efficiency with low toxicity and high payload. Here, we utilized NDs for the delivery of antimiRs targeting miR-155 (PNA-155) and 210 (PNA-210). We performed comprehensive evaluation of loading capacity, size, morphology and efficacy of antimiR-155- and 210 PNA-containing bicelles. Additionally, we performed molecular modeling, and Small-angle X-ray scattering (SAXS) to evaluate the interaction of hydrophobic PNAs with lipid. We further analyzed the transfection efficiencies of these NDs in cervical cancer cells (HeLa). We have also comprehensively evaluated the cellular uptake mechanism of bicelles containing antimiR

PNAs in HeLa cells. Our results highlight efficient and safe bicelle-mediated delivery of PNAs that can be used effectively for extensive biomedical applications.

MATERIAL AND METHODS

2.1 Materials

The zwitterionic short-chain dihexanoyl phosphatidylcholine (di-6:0, DHPC) lipid, and zwitterionic long-chain dipalmitoyl phosphatidylcholine (di-16:0, DPPC) lipid, negatively charged long-chain dipalmitoyl phosphatidylglycerol (DPPG), 1,2-dipalmitoyl-3-trimethylammonium-propane (chloride salt) (DOTAP), and polyethylene glycol (PEG2000)-conjugated distearoyl phosphoethanolamine (DSPE-PEG2000) were purchased from Avanti Polar Lipids (Alabaster, AL, USA). They are used without further purification. Phosphate buffered saline (PBS) powder was purchased from Sigma-Aldrich (St. Louis, MO). Dulbecco's Phosphate-Buffered Saline (DPBS) was purchased from Life Technologies (Grand Island, NY, USA). Boc-protected PNA monomers used for PNA synthesis were purchased from ASM Chemicals and Research (Hanover, Germany). Boc-MiniPEG and Nα-t-Butyloxycarbonyl-Nγ-Benzyloxycarbonyl-L-Lysine (Boc-Lys(Z)-OH) were purchased from Peptides International (Kentucky, USA). Boc-5-carboxytetramethylrhodamine (TAMRA) dye was purchased from VWR (Radnor, Pennsylvania). Chlorpromazine, Amiloride and Genistein were purchased from Sigma-Aldrich (MO, USA). human embryonic kidney (HEK) cells (ATCC® CRL-1573™) were purchased from ATCC (Virginia, USA). CellTiter 96® Aqueous One Solution Cell Proliferation Assay (MTS) was purchased from Promega (WI, USA).

2.2 Synthesis of folate conjugated Lipid NPs of different shapes

DPPC, DHPC, and DSPE-PEG2000, as well as either negatively charged DPPG or positively charged DOTAP were used for NPs preparation. The mixture, DPPC/DHPC/DPPG/DSPE-PEG2000 was prepared at a molar ratio of 69.58/25.1/3.76/2.0 [23].

All lipid molecules of the required weights were first homogenized in chloroform. After the removal of the solvent by a vacuum oven, the dried samples were then re-dispersed in filtered deionized (DI) water to make stock suspensions with a total lipid weight concentration, $C_{lp,}$ of 10% (wt). After successive vortex and temperature cycling between 25°C and 70°C, the stock dispersions were then progressively diluted at room temperature to C_{lp} = 1.0 mg/ml with PBS solution.

The PNA-entrapped bicelles were prepared at PNA:lipid molar ratios of 1:200, 1:500, 1:1000 and 1:2500, homogeneously dispersed in chloroform. After being dried, the sample was re-hydrated in water to form 10 wt.% mother solution by a proper temperature cycling and vortexing. The solution was then centrifuged at 10,000 rpm for 10 minutes in a Beckman Counter centrifuge to separate the aggregates and large particles and diluted to the desired concentration prior to the use for studies.

2.3 Measure the loading of antimiRs in NDs.

In order to investigate the encapsulation efficiencies of the PNAs, aqueous solutions of the bicelle encapsulated PNAs were diluted to 0.1 wt.% lipid concentration and centrifuged at 10000 rpm for 15 minutes. The top supernatant was separated as the encapsulated portion. The precipitates also were used to confirm the amount of non-encapsulated PNAs. Both supernatants and precipitations were dried under Nitrogen gas and redispersed accordingly with DMSO. After separating the precipitation and supernatant, the UV-visible absorption spectra (190–800 nm) of all samples were recorded by a Cary 5000 UV-Vis-NIR spectrometer (Agilent, USA). The absorbance of lipid compositions and PNA molecules alone were also used for the pre-calibrated curves and extinction coefficient confirmation. The encapsulation efficiencies (EE) of encapsulated PNAs in each sample was measured via the equation below:

$$\mathrm{EE} = \frac{[(\mathrm{OD} \times \mathrm{Mw} \times \text{dilution factor})/\varepsilon]}{\text{Initial Concentration}} \times 100,$$

where OD, Mw, ε are optical density (normalized absorbance intensity) and molecular weight of the PNA, extinction coefficient, respectively, dilution factor is 1000, and Initial concentration is in the unit of 0.01 wt.% of lipid nanocarrier.

2.4 Small angle X-ray scattering (SAXS)

SAXS measurements were conducted at 16ID-LiX Beamline at National Synchrotron Light Source II located at the Brookhaven National Laboratory (Upton, NY), using the standard flow-cell-based solution scattering setup with the X-ray energy of 13.5 keV. The SAXS intensity is expressed as a function of the scattering vector, q ($q \equiv \frac{4\pi}{\lambda} sin\frac{\theta}{2}$, where θ is the scattering angle) varies from 0.005 to 2.5 Å^{-1} [30]. Radial averaging and q-conversion of data were performed using the standard software [31] merging data from all three detectors used in the measurements. The transmission correction and background subtraction were performed to minimize the intensity of the hydrogen bond from water at ~2.0 Å^{-1}.

2.5 Dynamic light scattering (DLS)

Size and population distribution of pristine and PNA-encapsulated nanodiscs were also determined by ALV/CGS-8F/4 (*ALV* compact system, Germany) instrument at a 632.8 nm laser beam. The samples were dissolved and homogenized in filtered DI water to 0.1 wt%. The results were reported as the average of 10 measurements.

2.6 Transmission electron microscopy (TEM)

Negatively-stained transmission electron microscopic (TEM) images were obtained using FEI Tecnai T12. The samples were prepared by spreading 5 μL 0.001 wt.% solution on a 400 mesh Formvar/carbon film copper grid (Electron Microscopy Sciences, PA, USA) and negative

staining was applied with 10 mg/mL of Uranyl acetate (SPI Supplies, PA, USA). The grids were then dried at 25℃. The accelerating voltage of the TEM was set at 80 kV.

2.7 Atomic Force Microscopy (AFM) analysis

A 0.01 wt.% solution of the ND (-) PNA155 1:2500 was freshly made and were put on a freshly cleaved mica and dried. Soft silicon nitride cantilevers (Bruker Nano, Camarillo, CA) with silicon nitride tips were used with a nominal tip radius was 2 nm. Experiments were performed at room temperature, using an MFP-3D-BIO AFM (Asylum Research, Santa Barbara, CA), in contact mode with a scanning rate of 0.7 Hz.

2.8 Calculation of molecular lipophilic surface potential (MLSP).

MLSP describes the 3-D lipophilic influence of all fragments of a molecule [32] and can be calculated at given points in space [33]. MLSP analysis of the PNA 155-TAMRA and PNA 210-TAMRA molecules were carried out using the Molinspiration Property Calculation Service molecular modeling package in order to study the feasibility of encapsulation of them inside the lipid bilayers of nanodiscs [34]. The Gasteiger –Hückel charges were assigned to the atoms of TMS structure, and surfaces were generated. The color ramp for the MLSP ranges from violet/blue color representing the higher lipophilic potential (LP) to the red color representing the lower LP.

2.9 AntimiR-PNA based oligomers

PNA-155 and PNA-210 were synthesized via solid phase synthesis using MBHA (4-Methylbenzhydrylamine) resin and Boc-monomers (A, T, C, G)[35]. TAMRA dye was conjugated to N-terminus of PNAs with Boc-miniPEG-3 linker (OOO). PNAs were then cleaved from the resin using cleavage cocktail containing m-cresol: thioanisole: trifluoromethanesulfonic acid (TFMSA): trifluoroacetic acid (TFA) (1:1:2:4) followed by precipitation using diethyl ether. PNAs

were purified and characterized using reverse-phase high-performance liquid chromatography (HPLC) and matrix-assisted laser desorption/ionization–time of flight (MALDI–TOF) spectroscopy respectively. The concentration of PNAs was determined using UV-vis spectroscopy, and extinction coefficient of PNAs was calculated using extinction coefficient of individual monomers (13,700 $M^{-1}cm^{-1}$ (A), 6,600 $M^{-1}cm^{-1}$ (C), 11,700 $M^{-1}cm^{-1}$ (G), and 8,600 $M^{-1}cm^{-1}$ (T)) of the sequence.

PNA sequences used in the study are:

PNA-155-TAMRA: 5' TAMRA-ooo-ACCCCTATCACGATTAGCATTAA-Lys 3'

PNA-210-TAMRA: 5' TAMRA-ooo-TCAGCCGCTGTCACACGCACAG-Lys-3'

3.0 Confocal microscopy

Approximately 100,000 HeLa cells (ATCC® CCL-2™) were allowed to seed overnight on coverslips in 12 well plates. Cells were treated with only PNA-155-TAMRA, and PNA-155-TAMRA or PNA-210-TAMRA entrapped in optimized NDs (1:2500(-)) overnight. Amount of PNA-155-TAMRA used was kept at the same level as PNA-155-TAMRA entrapped in nanodiscs. After 24 hours, cells were gently washed with 1 mL phosphate buffered saline (PBS) (4X) at room temperature (RT). Further, the cells were fixed by adding 1 mL of 4% paraformaldehyde at 37°C for 10 minutes. After washing the cells with 1 mL PBS (2X), cells were permeabilized using 1 mL of 0.1% Triton-X in PBS at 37°C for 10 minutes. Cells were mounted on a slide using ProLong™ Diamond Antifade Mountant with DAPI (Life Technologies, Carlsbad, CA, USA). Samples were allowed to harden at 4°C overnight and images were taken using a Nikon A1R spectral confocal microscope.

3.1 Flow cytometry analysis

Approximately 100,000 HeLa cells (ATCC® CCL-2™) were seeded in 12 well plates overnight followed by treatment with PNA-210-TAMRA or PNA-155-TAMRA containing NDs for 24 hours. Cells were then washed with PBS (4X), and trypsinization was done using 0.25% trypsin-EDTA (Gibco®, Life Technologies) at 37°C for 4 minutes. Trypsinized cells were suspended in 1mL of DMEM, 10% FBS media and centrifuged at 1000 RPM for 4 minutes at 4°C. Further, the cells were washed twice with 1 mL of PBS at 1000 RPM for 4 minutes at 4°C. Fixation of cells was done using 300μL of 4% paraformaldehyde and flow cytometry was done using LSR Fortessa X-20 Cell Analyzer (BD Biosciences, San Jose, CA). Results obtained were analyzed using FlowJo analysis software.

3.2 Real-time PCR studies

RNA was extracted from HeLa cells (ATCC® CCL-2™) treated with PNA-155-TAMRA and nanodiscs containing PNA-155-TAMRA using RNeasy Mini Kit (Qiagen, Hilden, Germany). TaqMan™ MicroRNA Assay (Assay ID: 467534_mat) (Applied Biosystem, Foster City, CA) was used to measure miR-155 levels. cDNA was synthesized using miR-155 reverse transcriptase (RT) primers (TaqMan™ MicroRNA Assay), 10X RT buffer, 100 mM dNTPs in the presence of RNase inhibitor (Applied Biosystem, Foster City, CA). Reverse transcription was done under the conditions (16°C for 30 minutes, 42°C for 30 minutes, 85°C for 5 minutes) provided with TaqMan™ MicroRNA Assay using the thermal cycler (T100™, Bio-Rad, Hercules, CA).
MiR-155 specific primers (TaqMan™ MicroRNA Assay) and TaqMan™ Universal Master Mix II, with UNG (Applied Biosystem, Foster City, CA) were used under the conditions specified in the assay (50°C for 2 minutes, 95°C for 10 minutes, (95°C for 15 seconds, 60°C for 60 seconds)×40 cycles) for amplification of cDNA. U6 snRNA (TaqMan™ microRNA Control) assay was used as a control. No template control was used for both the U6 snRNA and miR-155 expression levels.

3.3 Endocytosis inhibitor Study

HeLa cells were incubated with chlorpromazine (10 μg/mL), amiloride (10 mM) and genistein (200 μmol/l) at 37°C. After 30 minutes, cells were treated with PNA-155-TAMRA bicelles at a dose of 4 μM/ml for one hour at 37 °C. Further, cells were washed with PBS and fixed using 4% paraformaldehyde followed with analysis by LSR Fortessa X-20 Cell Analyzer (BD Biosciences, San Jose, CA). For confocal microscopy, cells pre-treated with endocytosis inhibitors for 30 minutes, were incubated with PNA-155-TAMRA bicelles for one hour. After washing and fixing with 4% paraformaldehyde, cells were mounted in ProLong™ Diamond Antifade Mountant with DAPI (Life Technologies, Carlsbad, CA, USA). Images were taken by nikon A1R spectral confocal microscope.

3.4 Safety study in primary cells

Human embryonic kidney (HEK) 293 cells (2000 cells/well) were seeded overnight in 96 well plates. Cells were treated with PNA-155-TAMRA bicelles in dose dependent manner (1μM/ml, 2μM/ml, 4μM/ml ,6μM/ml and 8μM/ml) and incubated at 37°C. After 24 hours, cells were washed with PBS and incubated in fresh culture medium with 20 μl of MTS reagent (CellTiter 96® Aqueous One Solution Cell Proliferation Assay) at 37°C. After an hour, absorbance was measured at 490 nm and used to calculate % cell viability.

3.5 Westren blot analysis

HeLa cells were treated with NDs and protein was extracted with Radio-Immunoprecipitation Assay lysis buffer. Total protein of 50–100 mg was run on SDS/polyacrylamide gel electrophoresis gels and transferred to nitrocellulose membranes. Antibodies used were: Anti-p53 Antibody (DO-1) (SCBT - Santa Cruz Biotechnology, sc-126) at 1:500 and Anti-β-Actin

antibody (Sigma, A5316) at 1:10,000.

RESULTS

To assess that PNAs sequences will affect their encapsulation and characteristics in bicelles, we developed and optimized the delivery systems for two potential antimiRs: PNA-210 and 155 targeting miR-210 and 155 respectively. miR-210 is upregulated in almost all solid tumors, including breast, cervical, pancreatic, and colorectal cancer[36]. Similarly, miR-155 is upregulated in lymphoma as well as leukemia[37,38]. We tested PNA-carboxytetramethylrhodamine (TAMRA) conjugates that can be used both for imaging and efficacy studies.

Lipid-based bicellar formulations

First, we formulated positively and negatively charged bicelles (or NDs) to evaluate their antimiR PNA payload properties. In parallel, we compared three formulations comprising different PNA: lipid molar ratio; 1:2500, 1:1000 and 1:200. NDs were formulated based on established protocol. We did not notice any significant decreases in reaction yield during NDs formulation process containing antimiR PNAs.

NDs characterizations

We measured the distribution of hydrodynamic radii (R_H) of antimiRs loaded and pristine bicelles using a dynamic light scattering (DLS) method. In the pristine NDs, a radius of ~8.5 nm was observed that is consistent with the literature[21,23]. However, we noticed an increase in R_H for antimiR PNA loaded negatively-charged bicelles regardless of their surface charge (**Fig 1A**). For the samples with PNA: lipid molar ratios of 1:2500 and 1:1000, the RHs remain less than ~15 nm with a uniform distribution (**Fig S1**), while as the PNA: lipid molar ratio reaches 1:100, the R_H increases significantly with a broader distribution, implicative of PNA-induced irregularity. Further, our results showed similar size and uniformity for both PNAs, i.e., antimiR PNA-155

and PNA-210, at corresponding compositions, implying that the negatively-charged bicelle is capable of encapsulating the antimiR regardless of their nucleobase sequence composition. In contrast to the negatively charged bicelles, the positively charged bicelles result in large aggregates even at PNA: lipid ratios of 1:1000 and 1:2500, unlikely to fully retain the nanodiscoidal shape. Apparently, the electrostatic interaction between positive charge of bicelles and negative charge of PNA nucleobase interfered with the bicellar self-assembly.

Further, the morphologies of lipid/PNA complexes were examined by TEM and AFM. The TEM (**Fig. 1B and Fig S2**) and AFM images (**Fig. S3**) indicate uniform discoidal morphology for both PNA-210 and PNA-155 (PNA:lipid = 1:2500), respectively, as encapsulated in the negatively charged bicelles. The fact that no noticeable difference in shape and size is found for both systems agrees well with the prior DLS results. Nevertheless, antimiR PNA-210 loaded in positively-charged bicelles results in large vesicles (**Fig 1C**), also consistent with the DLS data.

Encapsulation efficiency

Incorporating hydrophobic small molecules trapped in the lipid bilayer of liposomes or biomimetic membranes has been investigated experimentally[39-42] and theoretically[43-45]. The encapsulation efficiencies for hydrophobic molecules in liposomes are generally not high[40,42]; however, it has been reported that the bilayer defects induced by the short-chain lipids enhance the activity of membrane to host lipophilic molecules[46]. It is expected that the encapsulation efficiency of hydrophobic molecules in bicelles is higher than in liposomes. Due to low solubility of PNAs in water, centrifugation is applied to the PNA-loaded bicelles to remove non-encapsulated PNA aggregates. In contrast to the colorless pristine bicelle solution, the PNA-encapsulated supernatants are pinkish depending on the concentration of encapsulated PNA. The entrapped amount of PNAs can be obtained from the UV-vis absorption spectra compared against a pre-calibrated UV-vis absorption spectrum, whose intensity is linearly dependent on the concentration of PNA (**see table 1 in supporting information**).

The encapsulation efficiencies (EE) of AntimiR PNA-210 and 155 encapsulated in bicelles are similar to each other at low PNA: lipid ratios **(Fig 2)**. However, with increased PNA: lipid ratio, the encapsulation efficiency decreased drastically (**Fig S4**). For instance, for a PNA: lipid ratio of 1:100, the EE is less than 10%, while with lower ratios, and 1:2500 the encapsulation rate in bicelles is 92±7, respectively (**Fig S4 and S5**). This further confirms that the lipophilicity of PNA allows for its interaction with bicelle, thus forming stable nanocomplex, and overwhelming insoluble PNA can be separated from the system through centrifugation. The fact that the centrifugation speed does not affect the experimental outcome of encapsulation efficiency as suggested by **Fig S6** indicates that the current centrifugation speed and time is sufficient to separate the encapsulated and unencapsulated PNAs.

Molecular modeling analysis of antimiR PNA sequences

The encapsulation mechanism of antimiR PNAs in bicelles can be understood through the analysis by the Molecular Lipophilicity Surface Potential (MLSP) and Molecular electrostatic potential (MEP) based methods (**Fig 3**), which were performed using VEGAZZ software. The analysis shows that TAMRA at the N-terminus of PNAs are more lipophilic and therefore can interact with the hydrophobic portion of the bicelles. However, PNA backbone contains scattered hydrophilic domains, which could be exposed to the aqueous environment outside of the bicelles. The following SAXS analysis will provide some insight into the location of PNA in bicelles.

SAXS analysis results

SAXS analysis allows structural characterizations through simulating the electron density distribution of formulated bicelles. SAXS measurements were performed on pristine bicelles, PNA-155-loaded and PNA-210-loaded bicelles with different PNA:lipid ratios and surface charges as shown in **Fig. 4** (additional results are provided in the supplementary **Fig. S7, S8**

and S9). The lipid concentration of all samples is 1.0 wt.%. In all the PNA encapsulated bicelles, the general scattering feature contains a broad peak between q = 0.06 and 0.20 $Å^{-1}$, originated from the regular spacing between the phosphate headgroups of the two leaflets where the electron density is higher than that of the acyl chains. Therefore, the electron density profile across the bilayer (i.e., water - head group shell -hydrocarbon core - head group shell - water) can be considered as a "square well" [21,47]. The broad peak in all SAXS patterns suggests that the lipids remain a bilayer structure.

A core-shell discoidal model (CSD model in supporting information) is employed to describe the bicelles [21-23], where the core and shell represent the hydrophobic lipid tails and hydrophilic phosphate headgroups, respectively. The best fitting parameters used in the model for the SAXS data enlisted in **Table 1**. R_{core} and ρ_{core} represent the radius and the electron density of the hydrophobic core, respectively, while t_{shell} and ρ_{shell} are the thickness and electron density of phosphate shells along normal of the bilayer, respectively. The rim has a thickness and electron density of t_{rim} and ρ_{rim}, respectively. The electron density of water, ρ_w is fixed throughout the fitting procedure. Moreover, we found the best fitting t_{shell} did not vary and thus was kept constant as well. The initial guesses of the electron densities used in the model were from the literature values for lipid bilayer nanoparticles elsewhere[21,48]. The CSD model can describe SAXS data well in *q*-range between 0.005 and 0.35 $Å^{-1}$. SAXS data at higher *q* values involve detailed structures in the bilayer (e.g., the contrast between methylene and methyl groups) smaller than 1.8 nm which is not considered in the current model. Although the SAXS data of bicelles (referred as to be "ND" representing nanodiscs) and PNA-loaded NDs seem to be similar. The comparison between the best fit of pristine ND and PNA-loaded SAXS data (individual plots at the bottom of **Fig. 4**) shows significant differences**.** The general conclusion of the best fitting procedure indicates the encapsulation of the antimiR-PNAs has no significant structural disturbance on the discoidal geometry, while some variation in the dimensions of the ND is found and will be discussed below.

The most drastic structural variation is the increase of total diameters for PNA-loaded ND, changing from 244 Å to 300 ~ 400 Å presumably caused by two factors: enlarged R_{core} and t_{riml}. The best fitting results show that R_{core} has less than 50% of increase while t_{rim} increases by more than 70%. Most interestingly, the best fitting shell (t_{shell}) and core (t_{core}) thicknesses are practically invariant. Further analysis on the best fitting t_{rim} (**Fig S8**) suggests that the range of t_{rim} has to be larger than 45 Å for all PNA-loaded NDs (50 - 55 Å for ND PNA 210 at 1:500, 45 – 51 Å for PNA 210 at 1:2500 and 48 – 55 for PNA 155 at 1:2500). The invariant bilayer thickness ($2t_{shell}+ t_{core}$) and significant increase of t_{rim} suggest that the entrapped PNA molecules are mainly located at the rim of the ND. A reasonable explanation is that the hydrophobic portion of the PNA (the highly lipophilic TAMRA group) anchors into the bicelles rim, resulting in the noticeable increase of rim thickness and the planar bilayer of the discs remains unchanged as the pristine bicelles.

Cellular uptake studies

Further, cellular uptake of formulated NDs was tested using TAMRA conjugated PNA-155 and PNA-210 antimiRs. Flow cytometry analysis was performed to quantify cellular uptake. HeLa cells were treated with positively as well as negatively charged bicelles containing antimiR PNAs (PNA: lipid molar ratio of 1:2500) for 24 h followed by flow cytometry analysis. We noticed the percentage of cells exhibiting fluorescence was significantly higher in the case negatively charged bicelles (~95%) as compared to positively charged one (~43%) **(Fig 5).** This is most likely due to the morphological difference, i.e., small uniform discoidal bicelles (negatively charged) compared to a mixture of bicelles and veiscles (positively charged). In addition, the fluorescence signal was significantly higher in cells (higher cellular uptake) treated with negatively charged bicelles containing PNA-155-TAMRA as well as PNA-210-TAMRA **(Fig 5 and 6)**. No auto fluorescence was observed in the un-transfected cells in the TAMRA channel.

Next, cellular uptake of negatively charged bicelles containing PNA-155-TAMRA and PNA-210-TAMRA was confirmed using confocal microscopy. HeLa cells treated PNA-155-TAMRA and PNA-210-TAMRA alone (same dose as present in the PNA-210 and PNA-155 bicelles) were used as control. HeLa cells in logarithmic phase were cultured in complete media and incubated with bicelles. After 24 h of incubation, cells were briefly washed three times with buffer saline and stained with nuclear dyes followed by imaging. As shown in **Fig 7**, bicelles containing PNA-155-TAMRA and PNA-210-TAMRA showed a narrow distribution of TAMRA signal in comparison to antimiR PNAs alone. Though we noticed significant distribution of PNA-TAMRA in the cytoplasm, we noted only few puncta of TAMRA in the nuclei of cells treated with ND (-) PNA-155 containing TAMRA. In parallel, cellular uptake analysis of PLGA nanoparticles containing antimiR PNA-155-TAMRA was also performed in HeLa cells. Bicelles showed not only a dramatic increase but also more uniform uptake as compared to punctate distribution by PLGA NPs (**Fig S10**). Together, these results show that negatively charged bicelles contribute to uniform and high transfection efficiency of antimiR PNAs in the cells. In order to asses the toxicity of bicelles we perfomed dose dependent MTT assay HEK293 primary cells. Minimal toxicity is noted as compred to the control samples (**Fig S11)**. In addition, we also investigated the cellular uptake mecahanism of negatively charged bicelles containing antimiR PNA-155-TAMRA.

Mechanism of cellular uptake

We performed comprehensive studies to to understand the cellular uptake mechanism of negatively charged bicelles containing antimiR PNAs. First, we investigated if endocytosis plays a significant role in the bicelles containing antimiR PNAs by performing temperature (37^{o}C vs 4^{o}C) dependent cellular uptake studies in HeLa cells. It has been proven that low temperature (4^{o}C) inhibits the endocytosis based transport across the cell membrane[49]. Our confocal microscopy and flow cytometry results revealed that NDs cellular uptake decreased significantly

at 4^{o}C (**Fig S12**).

Further, three pharmacological inhibitors of major endocytic pathway were used to study the cellular uptake mechanisms of negatively charged bicelles containing antimiR PNAs-155 in HeLa cells. Amiloride was used to inhibit the membrane ruffling and macropinocytosis[50]. Chlorpromazine (CPZ) was employed to block clathrin mediated endocytosis[51]. Genistein was tested to inhibit clathrin independent endocytosis or caveolae mediated endocytosis[52]. Further, inhibitors concentrations were adjusted to achieve viability of HeLa cells (~95%) for 2 hours. Both flow cytometry analysis as well as confocal microscopy were used to evaluate the cellular uptake after treatment with inhibitors and bicelles. Our results indicate that negatively charged bicelles undergoes cellular uptake by multiple endocytotic pathways. We noted that majority of bicelles containing antimiR PNAs underwent endocytosis by caveolae mediated endocytosis as well as macropinocytosis followed by clathrin mediated endocytosis (**Fig S13).**

Quantification of antimiR activity of NDs in cell culture

Next, we investigated the antimiR-155 efficacy of formulated bicelles by quantitative RT-PCR analysis. For all experiments, cells treated with PNA-155 alone were used as controls. We tested the expression of miR-155 in HeLa cell lines using RT-PCR. HeLa cells exhibited overexpression of miR-155 and hence, we tested HeLa cell lines for comparing the efficacy of formulated negatively charged bicelles containing PNA-155 at PNA:lipid molar ratio of 1:2500. HeLa cells were treated with sufficient amount of negatively charged bicelles to achieve a dose of 4 μM PNA for 24 h. RNA was extracted and quantified by RT-PCR using U6 as a control. Unlike the control, PNA-155-TAMRA loaded negatively charged bicelles reduced miR-155 expression by ~50% (**Fig. 8**). These results signify the antimiR activity of bicelles containing antimiR PNAs. Further, we also measured the antimiR-155 effect at protein levels using western blot analysis. p53 acts as a tumor suppressor, and regulates cell division by inhibiting cells from

growing and proliferating in an uncontrolled way. It has been established that miR-155 upregulation decreases level of p53 protein[53]. Our results revealed that pretreatment of HeLa cells with NDs containing PNA-155 led to ~39% upregulation of p53 **(Fig S14).**

DISCUSSION

In spite the use of PNAs was reported more than three decades ago, cellular uptake of PNAs still circumscribes their broader clinical applications. In this work using comprehensive structural and biophysical characterizations, fluorescence, as well as functional cell-based assay we successfully demonstrated that lipid-based formulations can be used for delivery of therapeutically active PNAs. It is noteworthy that the lipids (PEG 2000-DSPE, DPPG DPPC and DHPC) used to constitute the bicelles are FDA-approved. We tested a series of positive and negative charge NDs containing different PNA: Lipid molar ratio. Our results indicate that negatively charged bicelles containing a 1:2500 molar ratio of PNA: Lipid (the least disturbed composition) exhibit uniform size as well as discoidal shape. First, we confirmed that 1:2500 ratio results in maximum encapsulation efficiency of two antimiRs, i.e., PNA-210 and PNA-155. Bicelles made of lipid with controlled size are attainable [23]. The PEGylated bicelles are very stable and only turn into vesicles of similar size through incubating at 55°C or above for several hours, confirmed by TEM, DLS, and SAXS[21]. They have long-term stability in aqueous solutions and therefore are suitable as delivery carriers for drugs, vaccines, and genes for a variety of diseases.

The non-spherical geometries such as rod-like and discoidal NPs have been proved to permeate deeper in mammary tumors greater than their spherical counterparts with similar hydrodynamic sizes [54,55]. It has also been reported that NDs have high diffusion and penetration properties in collagen-rich environment [56]. Presumably, the small dimension along their thickness dimension promotes the tumor penetration as compared with the symmetric structure of vesicles. Interestingly, recent mathematical modeling combined with *in vitro* and *ex-vivo*

experimentation demonstrated that discoidal geometries possessed the most favorable margination dynamics in the body[57]. Additionally, discoidal NPs show particular movement dynamics that favor the interaction with vessel wall more than spherical particles [25,58]. Though it has been demonstrated that positively charged NPs are internalized into cell favorably due to their strong interaction with the negatively charged phospholipid components of the cell membrane [59], their toxicity is also much higher. Hence, the negatively charged bicelles are also favorable in terms of safety as well as efficacy[25]. Our cell culture analysis did not show any noticeable toxicity.

Further, the morphology of PNA/bicelles was investigated using SAXS data analysis. The parameters of the Core-Shell Bicelle model, that best fits the SAXS data of bicelles, indicate axial shell thickness, radial shell thickness, core thickness and radius consistent with literature values for pristine bicelles[47]. No significant difference was found in the SAXS patterns of PNAs loaded bicelles (i.e., discoidal shape with invariant bilayer thickness) compared to that of the pristine bicelle except that the Guinier regime shifts to the lower q values, indicative of larger particles. The drastically increased rim thickness suggests that most of the entrapped PNAs are preferably localized at the rim region. The disc rim mainly composed of short-chain DHPC has a large spontaneous curvature and contains more defects, making it suitable to accommodate higher-curvature objects like large PNA ending domains[60]. Cell culture analysis substantiates that negative charge bicelles shows high transfection efficiency. We did not notice any punctated structure in the HeLa cells treated with bicelles indicating that a good portion of bicelles may not undergo endosomal entrapment and uniformly distribute the antimiR PNAs in the cells. In addition, that the fact that the negatively charged bicelles undergo cellular uptake by multiple endocytic mechanisms is also consistent with our previous report[20].

CONCLUSION

In conclusion, our data demonstrate that PNAs can be efficiently delivered by negatively charged bicelles. This approach can be used to effectively reduce the levels of miRNA expression via an antisense mechanism. Improvements in accessibility to molecular targets and increased specificity could further be increased by coating PNA loaded bicelles with specific peptides, antibody and carbohydrate units. In summary, this work provides a novel platform for PNA delivery that can be developed for therapeutic purposes. Results presented in this report can serve as a promising platform based on the PNA/bicelle technology to control the gene expression and regulation for diverse biomedical applications.

Statistical analysis.

Comparisons between two groups were carried out with Student's t-tests, Differences with P values of less than 0.05 were considered statistically significant.

Conflicts of Interest

The author declares no competing financial interests.

Acknowledgements

We thank Anisha Gupta for discussions and suggestions. This work was supported by University of Connecticut startup funds, UConn START PPOC award (RB) and A. T. R. is supported by NSF-CBET #1605971. The authors would like to acknowledge the beamtime of 16D-LiX at the NSLS-II (Brookhaven National Lab) through a beamtime proposal (BAG-302208). The LiX beamline is part of the Life Science Biomedical Technology Research resource, jointly supported by the National Institute of Health, National Institute of General Medical Sciences under Grant P41 GM111244, and by the Department of Energy Office of

Biological and Environmental Research under Grant KP1605010, with additional support from NIH Grant S10 OD012331. NSLS-II is a U.S. Department of Energy (DOE) Office of Science User Facility operated for the DOE Office of Science by Brookhaven National Laboratory under Contract No. DE-SC0012704. We also would like to thank Dr. Jing Zhang and Dr. George Lykotrafitis for their for scientific support on the AFM analysis. Also we acknowledge Justin M. Fang for the technical helps for TEM studies.

Author contributions

M.P.N, R.B, A.T.R, and S.M designed the research; A.T.R, and S.M. performed the research; S.M and T.K.O peformed western blot analysis; M.P.N, R.B, A.T.R, and S.M analyzed the data and wrote the paper; L.Y. set up the SAXS experiment.

Figures.

Fig. 1. **(A)** Size distribution of nanodiscs (ND) and nanovesicles in the presence (solid) and absence (dotted) folate ligand. The hydrodynamic radius, R_H of NPs was 10 ~ 12 nm for ND, consistent with the best fitting dimensions from SAXS data **(B and C)** TEM images of negative charge ND (-) and positive charge ND (+) containing lipid:PNA molar ratio of 1:2500 loaded with PNA-210. The planar and rim views are pointed by yellow and red arrows, respectively. The diameter of NPs was ~30 nm for ND, consistent with the best fitting dimensions of SAXS and the hydrodynamic radius measured by DLS. Scale bars in all images are equal to 100 nm.

Fig. 2. Encapsulation Efficiencies (EE) of antimiR-155 and 210 PNAs in negative charge containing NDs. The bar chart shows the encapsulation rates calculated by the ratio of encapsulated PNA molecules compared to the initial mass of PNA added. The line chart (right y-axis) indicates the highest achievable concentration of the PNAs encapsulated in NDs and stable in the aqueous phase.

Fig. 3. Simulation studies for the antimiR PNA molecules, using VEGAZZ® software. (A and B) Chemical structure of antimiR PNA-155 and 210. TAMRA is at the far left side of the structure. (C and D) Molecular electrostatic potential (MEP) of PNA-155 and 210. (E and F) MLSP analysis of PNA-155 and PNA 210. Moving from blue to red on the scale indicates increasing MLSP. Encircled red portions show lipophilic regions exposed on the surface of the molecules, which provides an ideal segment in the molecule to be incorporated into the lipid bilayer. Both PNA molecules show low lipophilicity and low hydrophilicity in the main backbone, while the TAMRA part is highly lipophilic structure. (G and I) A higher magnification of the TAMRA domains of AntimiR PNA molecules is also provided in parts. (H and J) indicate the multiple hydrophilic and hydrophobic domains of PNA backbone respectively.

Fig 4. SAXS results of antimiR-PNAs encapsulated in NDs. All the curves start with the Guinier region which reciprocally correlates with the size of the nanocarriers. The broad peaks at 0.07-0.2 1/Å belong to the headgroup distance of the phospholipid bilayers and bilayer thickness. Higher q peaks correlate with the internal nanostructures of the NDs. Below, best fitting results are shown for each sample. As shown, to make a clear comparison, the results for the pristine NDs are also plotted versus the ND-PNA nanocomplexes.

Fig 5. FACS analysis of HeLa cells following incubation with the negative ND (-) and positive ND (+) containing PNA-210. 2000 cells were selected for the number of events.

Fig 6. FACS analysis of HeLa cells following incubation with the negative ND (-) containing PNA-210 and PNA-155. 5000 cells were selected for the number of events.

Fig 7. Fluorescent images of HeLa cells incubated with negative charge containing NDs for 24

h, followed by brief washing with PBS and incubation with DAPI (Nuclear staining). Blue: nucleus (DAPI), Red: PNA (TAMRA).

Fig 8. miR-155 expression in HeLa cells after treatment with negative charge NDs containing PNA-155. miR-155 expression relative to average control (all normalized to U6, n = 3, *p < 0.05).

Table 1. The best-fitting parameters obtained from the SAXS data of the NDs

	Core-Shell Discoidal Model (with invariant t_{shell} = 14.9 Å, and ρ_w = 9.40 x 10^{-6} Å^{-2})						
	ρ_{shell}, ×10-6 Å^{-2}	ρ_{rim}, ×10-6 Å^{-2}	t_{rim}, Å	ρ_{core}, ×10-6Å^{-2}	t_{core}, Å	R_{core}, Å	Disc Diameter, Å
NDs	10.7 (±0.1)	9.8 (±0.1)	27.1 (±0.5)	7.1 (±1.1)	25.1 (±0.2)	95 (± 8)	244 (± 9)
ND(-)PNA 210 1:500	12.9 (±0.9)	9.9 (±0.6)	52.5 (±4.5)	7.1 (±2.2)	24.4 (±0.3)	148 (± 11)	400 (± 16)
ND (-)PNA 210 1:2500	12.6 (±0.4)	9.9 (±1.5)	47.8 (±2.9)	6.75 (±1.2)	24.8 (±0.7)	106 (± 1)	308 (± 4)
ND (-) PNA155 1:2500	10.7 (±1.7)	9.7 (±3.5)	51.8 (±2.8)	8.3 (±0.8)	24.6 (±0.6)	135 (± 2)	375 (± 5)

References

1 Egholm, M. *et al.* PNA hybridizes to complementary oligonucleotides obeying the Watson-Crick hydrogen-bonding rules. *Nature (London)* **365**, 566-568, doi:10.1038/365566a0 (1993).

2 Nielsen, P. E., Egholm, M., Berg, R. H. & Buchardt, O. Sequence-selective recognition of DNA by strand displacement with a thymine-substituted polyamide. *Science (Washington, D. C., 1883-)* **254**, 1497-1500, doi:10.1126/science.1962210 (1991).

3 Nielsen, P. E. Peptide nucleic acids: a new dimension to peptide libraries and aptamers. *Methods Enzymol* **267**, 426-433 (1996).

4 Demidov, V. V. *et al.* Stability of peptide nucleic acids in human serum and cellular extracts. *Biochem Pharmacol* **48**, 1310-1313 (1994).

5 Gupta, A., Bahal, R., Gupta, M., Glazer, P. M. & Saltzman, W. M. Nanotechnology for delivery of peptide nucleic acids (PNAs). *J Control Release*, doi:10.1016/j.jconrel.2016.01.005 (2016).

6 Bahal, R., McNeer, N. A., Ly, D. H., Saltzman, W. M. & Glazer, P. M. Nanoparticle for delivery of antisense gammaPNA oligomers targeting CCR5. *Artif DNA PNA XNA* **4**, 49-57 (2013).

7 Malik, S., Oyaghire, S. & Bahal, R. Applications of PNA-laden nanoparticles for hematological disorders. *Cell Mol Life Sci* **76**, 1057-1065, doi:10.1007/s00018-018-2979-5 (2019).

8 Malik, S., Asmara, B., Moscato, Z., Mukker, J. K. & Bahal, R. Advances in Nanoparticle-based Delivery of Next Generation Peptide Nucleic Acids. *Curr Pharm Des*, doi:10.2174/1381612825666190117164901 (2019).

9 Clarenc, J. P., Degols, G., Leonetti, J. P., Milhaud, P. & Lebleu, B. Delivery of antisense oligonucleotides by poly(L-lysine) conjugation and liposome encapsulation. *Anticancer Drug Des* **8**, 81-94 (1993).

10 Delgado, E. *et al.* beta-Catenin knockdown in liver tumor cells by a cell permeable gamma guanidine-based peptide nucleic acid. *Curr Cancer Drug Targets* **13**, 867-878 (2013).

11 Sahu, B. *et al.* Synthesis of conformationally preorganized and cell-permeable guanidine-based gamma-peptide nucleic acids (gammaGPNAs). *J Org Chem* **74**, 1509-1516, doi:10.1021/jo802211n (2009).

12 Coester, C., Kreuter, J., von Briesen, H. & Langer, K. Preparation of avidin-labelled gelatin nanoparticles as carriers for biotinylated peptide nucleic acid (PNA). *Int J Pharm* **196**, 147-149 (2000).

13 Bertucci, A. *et al.* Intracellular delivery of peptide nucleic acid and organic molecules using zeolite-L nanocrystals. *Adv Healthc Mater* **3**, 1812-1817, doi:10.1002/adhm.201400116 (2014).

14 Bertucci, A. *et al.* Combined Delivery of Temozolomide and Anti-miR221 PNA Using Mesoporous Silica Nanoparticles Induces Apoptosis in Resistant Glioma Cells. *Small* **11**, 5687-5695, doi:10.1002/smll.201500540 (2015).

15 Zhang, K., Fang, H., Wang, Z., Taylor, J. S. & Wooley, K. L. Cationic shell-crosslinked knedel-like nanoparticles for highly efficient gene and oligonucleotide transfection of mammalian cells. *Biomaterials* **30**, 968-977, doi:10.1016/j.biomaterials.2008.10.057 (2009).

16 Bahal, R. *et al.* In vivo correction of anaemia in beta-thalassemic mice by gammaPNA-mediated gene editing with nanoparticle delivery. *Nat Commun* **7**, 13304, doi:10.1038/ncomms13304 (2016).

17 Ricciardi, A. S. *et al.* In utero nanoparticle delivery for site-specific genome editing. *Nat Commun* **9**, 2481, doi:10.1038/s41467-018-04894-2 (2018).

18 Iqbal, U. *et al.* Small unilamellar vesicles: a platform technology for molecular imaging of brain tumors. *Nanotechnology* **22**, 195102, doi:10.1088/0957-4484/22/19/195102 (2011).

19 Nieh, M. P., Kucerka, N. & Katsaras, J. Spontaneously formed unilamellar vesicles. *Methods in Enzymology* **465**, 3-20, doi:10.1016/s0076-6879(09)65001-1 (2009).

20 Lyukmanova, E. *et al.* Lipid–protein nanodiscs for cell-free production of integral membrane proteins in a soluble and folded state: comparison with detergent micelles, bicelles and liposomes. *Biochimica et Biophysica Acta (BBA)-Biomembranes* **1818**, 349-358 (2012).

21 Liu, Y., Li, M., Yang, Y., Xia, Y. & Nieh, M.-P. The effects of temperature, salinity, concentration and PEGylated lipid on the spontaneous nanostructures of bicellar mixtures. *Biochimica et Biophysica Acta (BBA)-Biomembranes* **1838**, 1871-1880 (2014).

22 Aresh, W. *et al.* The Morphology of Self-Assembled Lipid-Based Nanoparticles Affects Their Uptake by Cancer Cells. *Journal of Biomedical Nanotechnology* **12**, 1852-1863 (2016).

23 Liu, Y., Xia, Y., Rad, A. T., Aresh, W. & Nieh, M.-P. Stable Discoidal Bicelles: A Platform of Lipid Nanocarriers for Cellular Delivery. *Liposomes: Methods and Protocols*, 273-282 (2017).

24 Muro, S. *et al.* Control of endothelial targeting and intracellular delivery of therapeutic enzymes by modulating the size and shape of ICAM-1-targeted carriers. *Molecular Therapy* **16**, 1450-1458 (2008).

25 Blanco, E., Shen, H. & Ferrari, M. Principles of nanoparticle design for overcoming biological barriers to drug delivery. *Nature biotechnology* **33**, 941-951 (2015).

26 Agarwal, R. *et al.* Mammalian cells preferentially internalize hydrogel nanodiscs over nanorods and use shape-specific uptake mechanisms. *Proceedings of the National Academy of Sciences* **110**, 17247-17252 (2013).

27 Tan, J., Shah, S., Thomas, A., Ou-Yang, H. D. & Liu, Y. The influence of size, shape and vessel geometry on nanoparticle distribution. *Microfluidics and nanofluidics* **14**, 77-87 (2013).

28 Chou, L. Y., Ming, K. & Chan, W. C. Strategies for the intracellular delivery of nanoparticles. *Chemical Society Reviews* **40**, 233-245 (2011).

29 Agarwal, R. *et al.* Effect of shape, size, and aspect ratio on nanoparticle penetration and distribution inside solid tissues using 3D spheroid models. *Advanced healthcare materials* **4**, 2269-2280 (2015).

30 DiFabio, J. *et al.* in *AIP Conference Proceedings.* 030049 (AIP Publishing).

31 Yang, L. Using an in-vacuum CCD detector for simultaneous small-and wide-angle scattering at beamline X9. *Journal of synchrotron radiation* **20**, 211-218 (2013).

32 Laad, P., Shete, G., Modi, S. R. & Bansal, A. K. Differential surface properties of commercial crystalline telmisartan samples. *European Journal of Pharmaceutical Sciences* **49**, 109-116 (2013).

33 Testa, B., Carrupt, P.-A., Gaillard, P., Billois, F. & Weber, P. Lipophilicity in molecular modeling. *Pharmaceutical research* **13**, 335-343 (1996).

34 Quijano, E., Bahal, R., Ricciardi, A., Saltzman, W. M. & Glazer, P. M. Therapeutic Peptide Nucleic Acids: Principles, Limitations, and Opportunities. *Yale J Biol Med* **90**, 583-598 (2017).

35 Christensen, L. *et al.* Solid-phase synthesis of peptide nucleic acids. *J. Pept. Sci.* **1**, 185-183, doi:10.1002/psc.310010304 (1995).

36 Gupta, A. *et al.* Anti-tumor Activity of miniPEG-gamma-Modified PNAs to Inhibit MicroRNA-210 for Cancer Therapy. *Mol Ther Nucleic Acids* **9**, 111-119, doi:10.1016/j.omtn.2017.09.001 (2017).

37 Babar, I. A. *et al.* Nanoparticle-based therapy in an in vivo microRNA-155 (miR-155)-dependent mouse model of lymphoma. Author summary. *Proc. Natl. Acad. Sci. U. S. A.* **109**, 10140-10141, doi:10.1073/pnas.1201516109 (2012).

38 Cheng, C. J. *et al.* MicroRNA silencing for cancer therapy targeted to the tumour microenvironment. *Nature* **518**, 107-110, doi:10.1038/nature13905 (2015).

39 Binder, W. H., Sachsenhofer, R., Farnik, D. & Blaas, D. Guiding the location of nanoparticles into vesicular structures: a morphological study. *Physical Chemistry Chemical Physics* **9**, 6435-6441 (2007).

40 Rasch, M. R. *et al.* Hydrophobic gold nanoparticle self-assembly with phosphatidylcholine lipid: membrane-loaded and janus vesicles. *Nano letters* **10**, 3733-3739 (2010).

41 Von White, G., Chen, Y., Roder-Hanna, J., Bothun, G. D. & Kitchens, C. L. Structural and thermal analysis of lipid vesicles encapsulating hydrophobic gold nanoparticles. *ACS nano* **6**, 4678-4685 (2012).

42 An, X., Zhan, F. & Zhu, Y. Smart photothermal-triggered bilayer phase transition in AuNPs–liposomes to release drug. *Langmuir* **29**, 1061-1068 (2013).

43 Van Lehn, R. C. *et al.* Lipid tail protrusions mediate the insertion of nanoparticles into model cell membranes. *Nature communications* **5**, 4482 (2014).

44 Van Lehn, R. C. & Alexander-Katz, A. Fusion of ligand-coated nanoparticles with lipid bilayers: Effect of ligand flexibility. *The Journal of Physical Chemistry A* **118**, 5848-5856 (2014).

45 Van Lehn, R. C. & Alexander-Katz, A. Pathway for insertion of amphiphilic nanoparticles into defect-free lipid bilayers from atomistic molecular dynamics simulations. *Soft Matter* **11**, 3165-3175 (2015).

46 Xia, Y. *et al.* Effects of Membrane Defects and Polymer Hydrophobicity on Networking Kinetics of Vesicles. *Langmuir* (2017).

47 Yang, P.-W., Lin, T.-L., Hu, Y. & Jeng, U.-S. Small-Angle X-ray Scattering studies on the structure of mixed DPPC/diC7PC micelles in aqueous solutions. *Chinese Journal of Physics* **50**, 349-356 (2012).

48 Albanese, A., Tang, P. S. & Chan, W. C. The effect of nanoparticle size, shape, and surface chemistry on biological systems. *Annual review of biomedical engineering* **14**, 1-16 (2012).

49 Vives, E., Brodin, P. & Lebleu, B. A truncated HIV-1 Tat protein basic domain rapidly translocates through the plasma membrane and accumulates in the cell nucleus. *J Biol Chem* **272**, 16010-16017 (1997).

50 Ivanov, A. I. Pharmacological inhibition of endocytic pathways: is it specific enough to be useful? *Methods Mol Biol* **440**, 15-33, doi:10.1007/978-1-59745-178-9_2 (2008).

51 Rejman, J., Bragonzi, A. & Conese, M. Role of clathrin- and caveolae-mediated endocytosis in gene transfer mediated by lipo- and polyplexes. *Mol Ther* **12**, 468-474, doi:10.1016/j.ymthe.2005.03.038 (2005).

52 Sahay, G., Alakhova, D. Y. & Kabanov, A. V. Endocytosis of nanomedicines. *J Control Release* **145**, 182-195, doi:10.1016/j.jconrel.2010.01.036 (2010).

53 Van Roosbroeck, K. *et al.* Combining Anti-Mir-155 with Chemotherapy for the Treatment of Lung Cancers. *Clin Cancer Res* **23**, 2891-2904, doi:10.1158/1078-0432.CCR-16-1025 (2017).

54 Chauhan, V. P. *et al.* Fluorescent nanorods and nanospheres for real-time in vivo probing of nanoparticle shape-dependent tumor penetration. *Angewandte Chemie* **50**, 11417-11420, doi:10.1002/anie.201104449 (2011).

55 Agarwal, R. *et al.* Mammalian cells preferentially internalize hydrogel nanodiscs over nanorods and use shape-specific uptake mechanisms. *Proceedings of the National Academy of Sciences of the United States of America* **110**, 17247-17252, doi:10.1073/pnas.1305000110 (2013).

56 Ng, K. K., Lovell, J. F., Vedadi, A., Hajian, T. & Zheng, G. Self-assembled porphyrin nanodiscs with structure-dependent activation for phototherapy and photodiagnostic applications. *ACS Nano* **7**, 3484-3490, doi:10.1021/nn400418y (2013).

57 Lee, H., Fonge, H., Hoang, B., Reilly, R. M. & Allen, C. The effects of particle size and molecular targeting on the intratumoral and subcellular distribution of polymeric nanoparticles. *Molecular pharmaceutics* **7**, 1195-1208 (2010).

58 Gentile, F. *et al.* The effect of shape on the margination dynamics of non-neutrally buoyant particles in two-dimensional shear flows. *Journal of biomechanics* **41**, 2312-2318 (2008).

59 Verma, A. & Stellacci, F. Effect of surface properties on nanoparticle-cell interactions. *Small* **6**, 12-21, doi:10.1002/smll.200901158 (2010).

60 Sharma, H. & Dormidontova, E. E. Lipid Nanodisc-Templated Self-Assembly of Gold Nanoparticles into Strings and Rings. *ACS nano* **11**, 3651-3661 (2017).

Fig 1

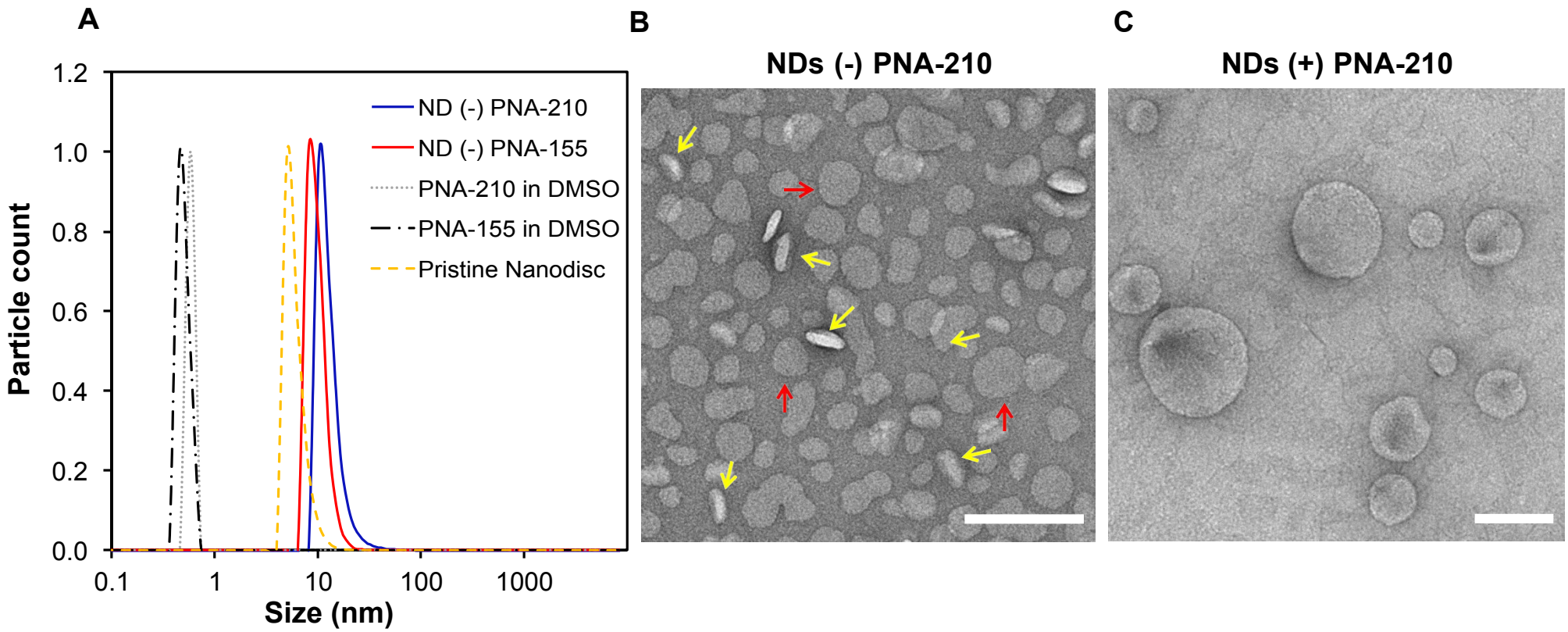
A
B
C
NDs (-) PNA-210
NDs (+) PNA-210
Particle count
Size (nm)
1.2
1.0
0.8
0.6
0.4
0.2
0.0
0.1
1
10
100
1000
ND (-) PNA-210
ND (-) PNA-155
PNA-210 in DMSO
PNA-155 in DMSO
Pristine Nanodisc

Fig 2

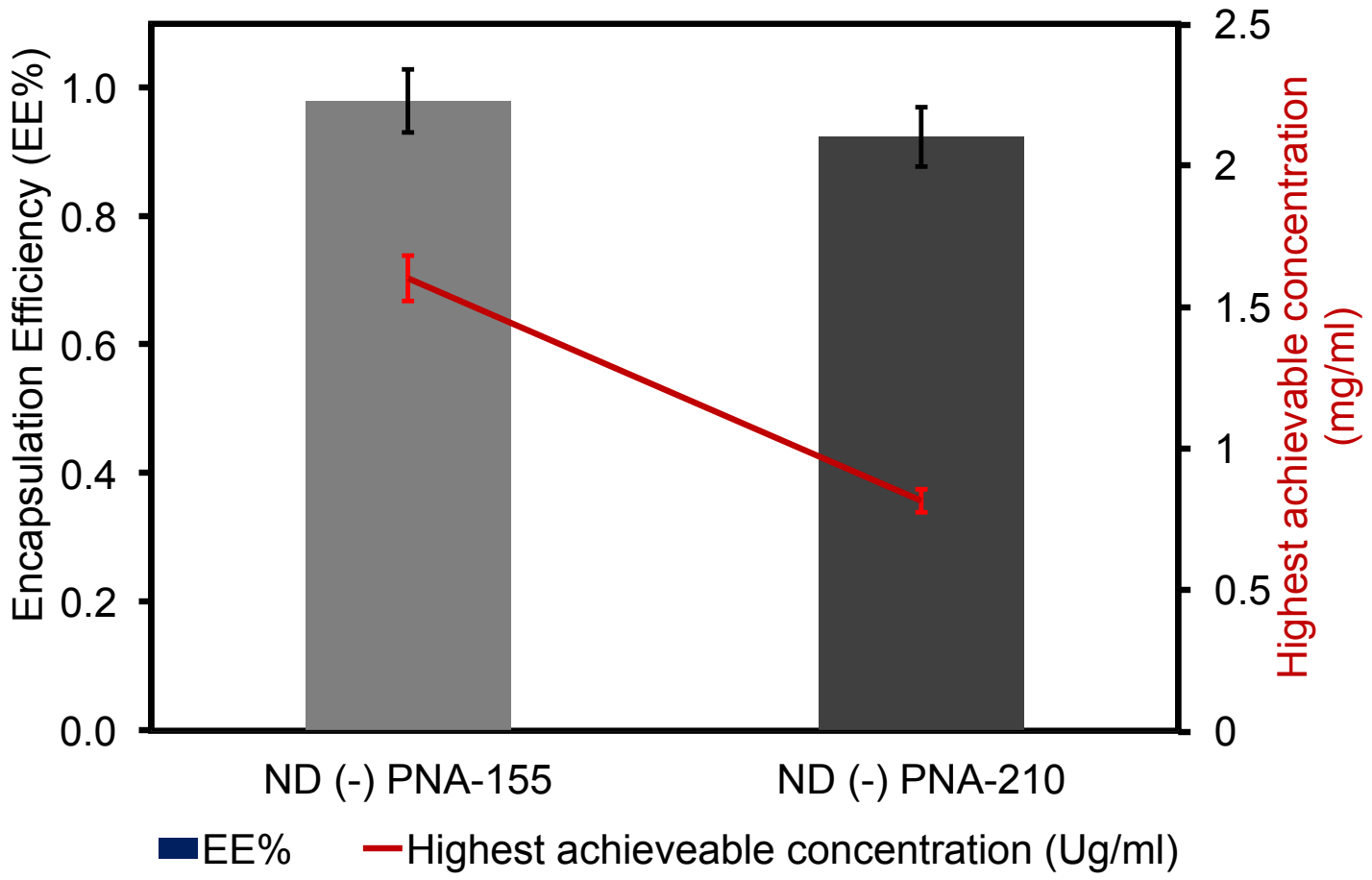
Encapsulation Efficiency (EE%)
1.0
0.8
0.6
0.4
0.2
0.0
2.5
2
1.5
1
0.5
0
Highest achievable concentration (mg/ml)
ND (-) PNA-155
ND (-) PNA-210
EE%
Highest achieveable concentration (Ug/ml)

Fig 3

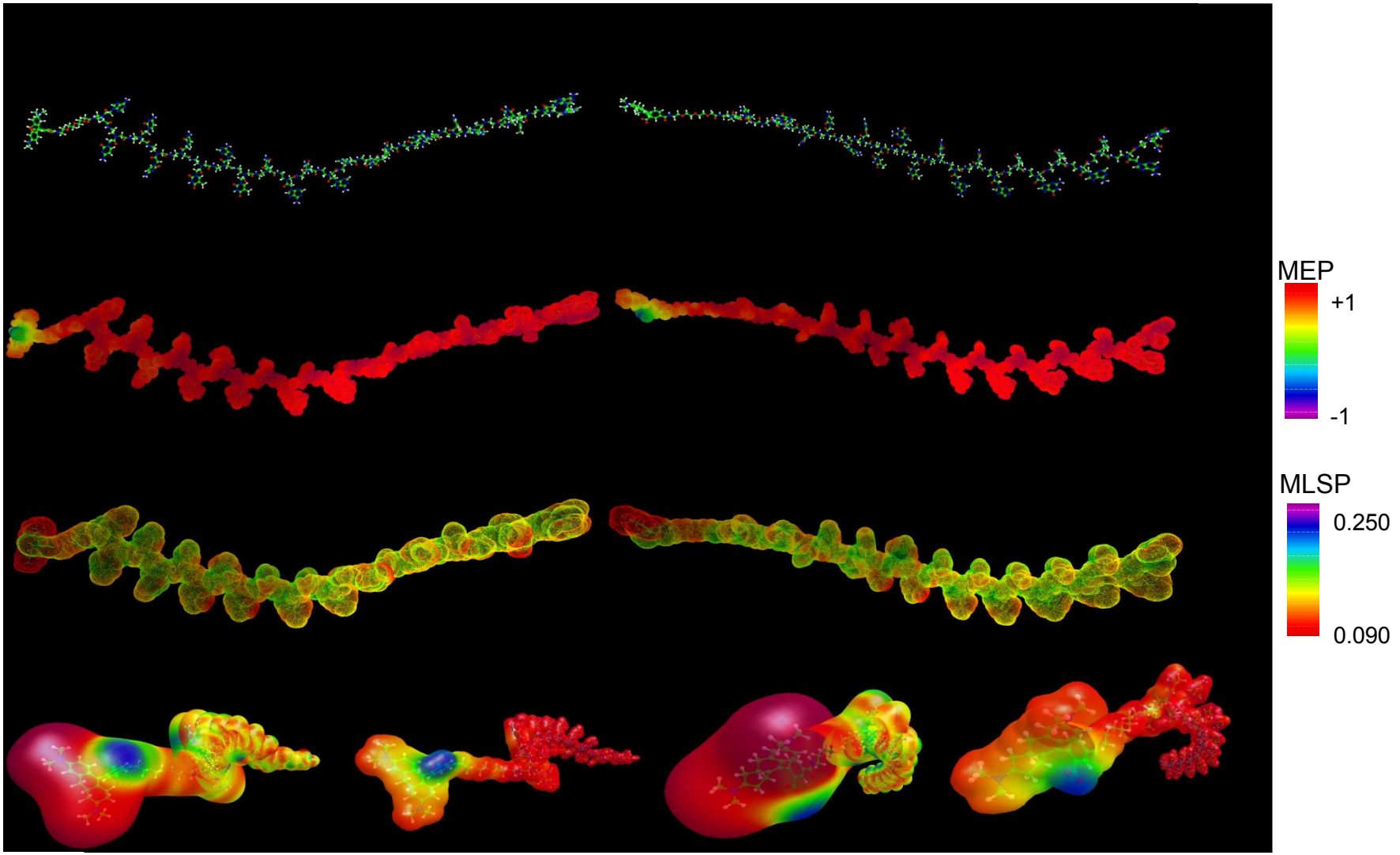

Fig 4

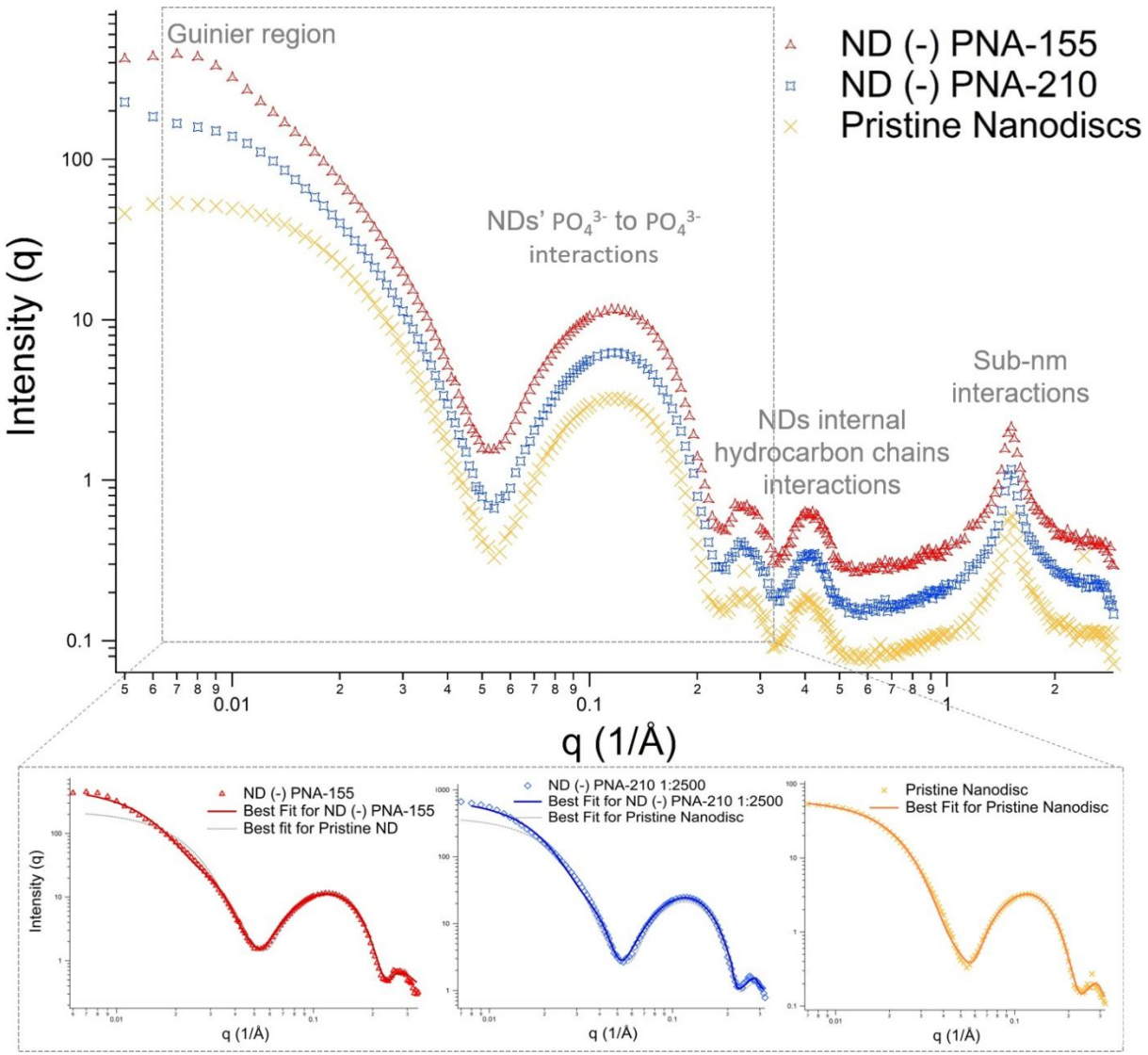
Guinier region
NDs' PO_4^{3-} to PO_4^{3-} interactions
NDs internal hydrocarbon chains interactions
Sub-nm interactions
ND (-) PNA-155
ND (-) PNA-210
Pristine Nanodiscs
Intensity (q)
q (1/Å)
ND (-) PNA-155
Best Fit for ND (-) PNA-155
Best fit for Pristine ND
ND (-) PNA-210 1:2500
Best Fit for ND (-) PNA-210 1:2500
Best Fit for Pristine Nanodisc
Pristine Nanodisc
Best Fit for Pristine Nanodisc

Fig 5

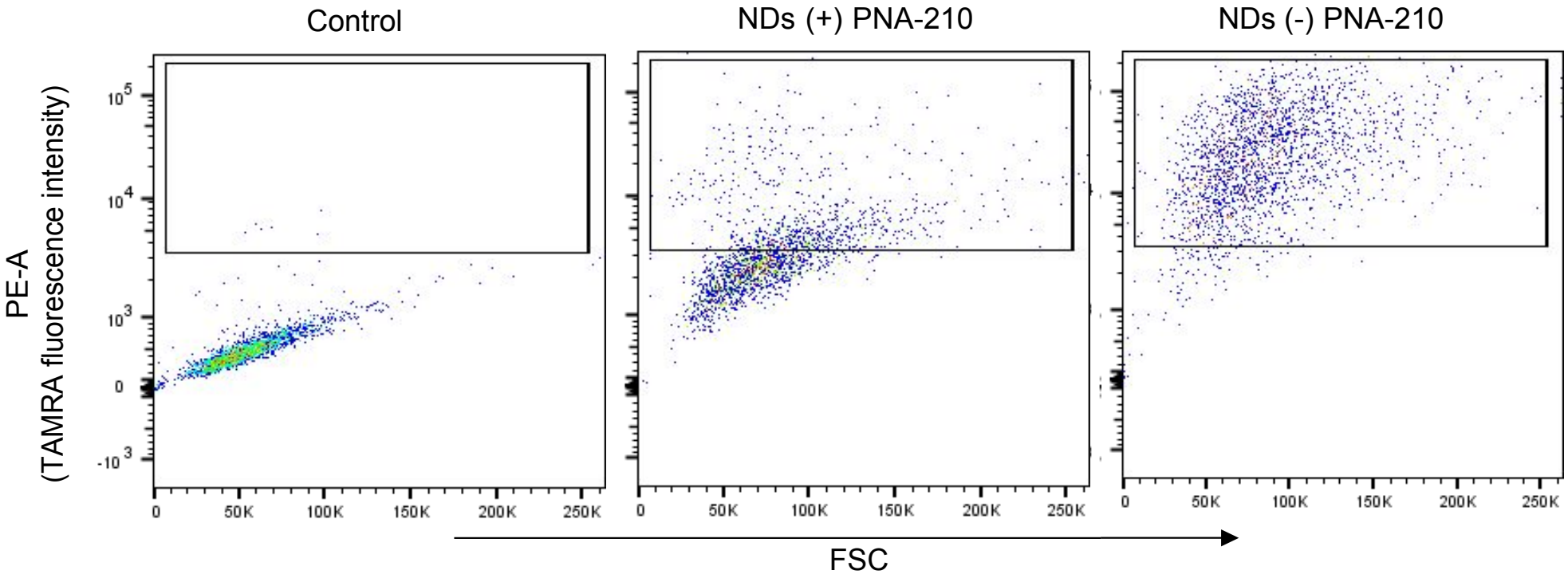
Control
NDs (+) PNA-210
NDs (-) PNA-210
PE-A
(TAMRA fluorescence intensity)
10^5
10^4
10^3
0
-10^3
0
50K
100K
150K
200K
250K
FSC

Fig 6

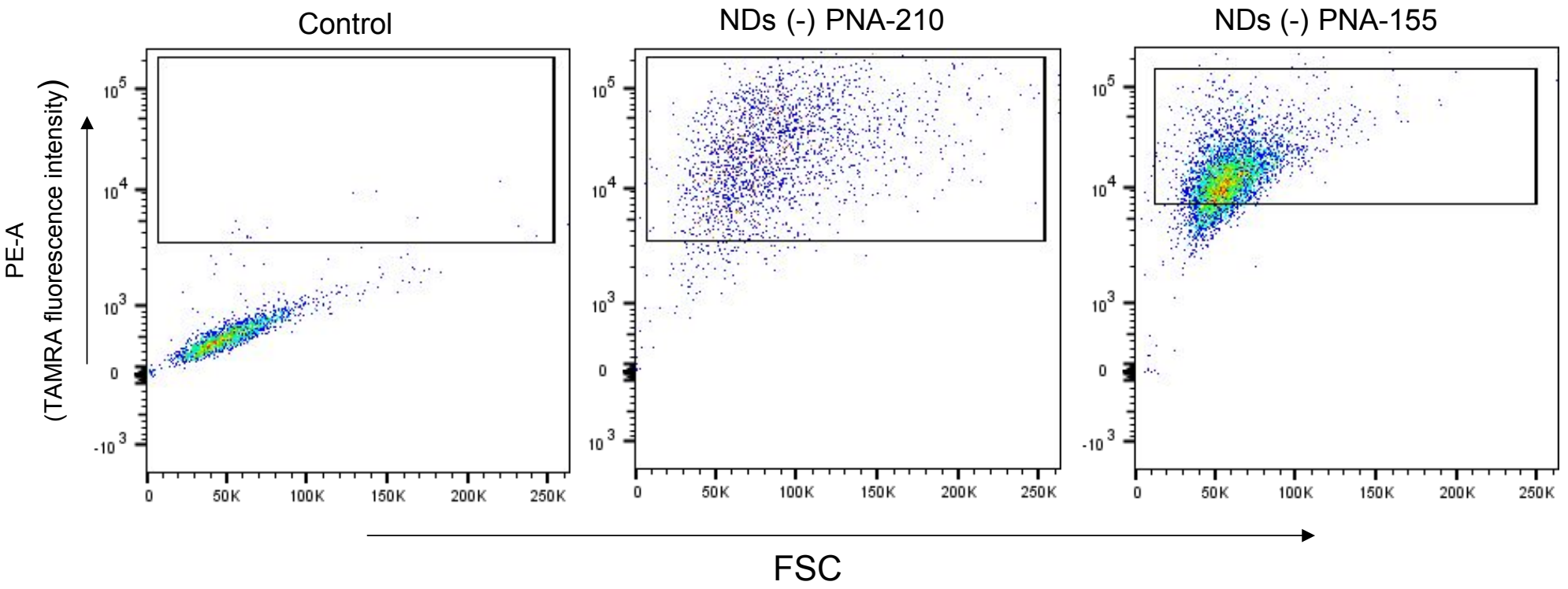
Control
NDs (-) PNA-210
NDs (-) PNA-155
PE-A
(TAMRA fluorescence intensity)
FSC
10^5
10^4
10^3
0
-10^3
0
50K
100K
150K
200K
250K

Fig 7

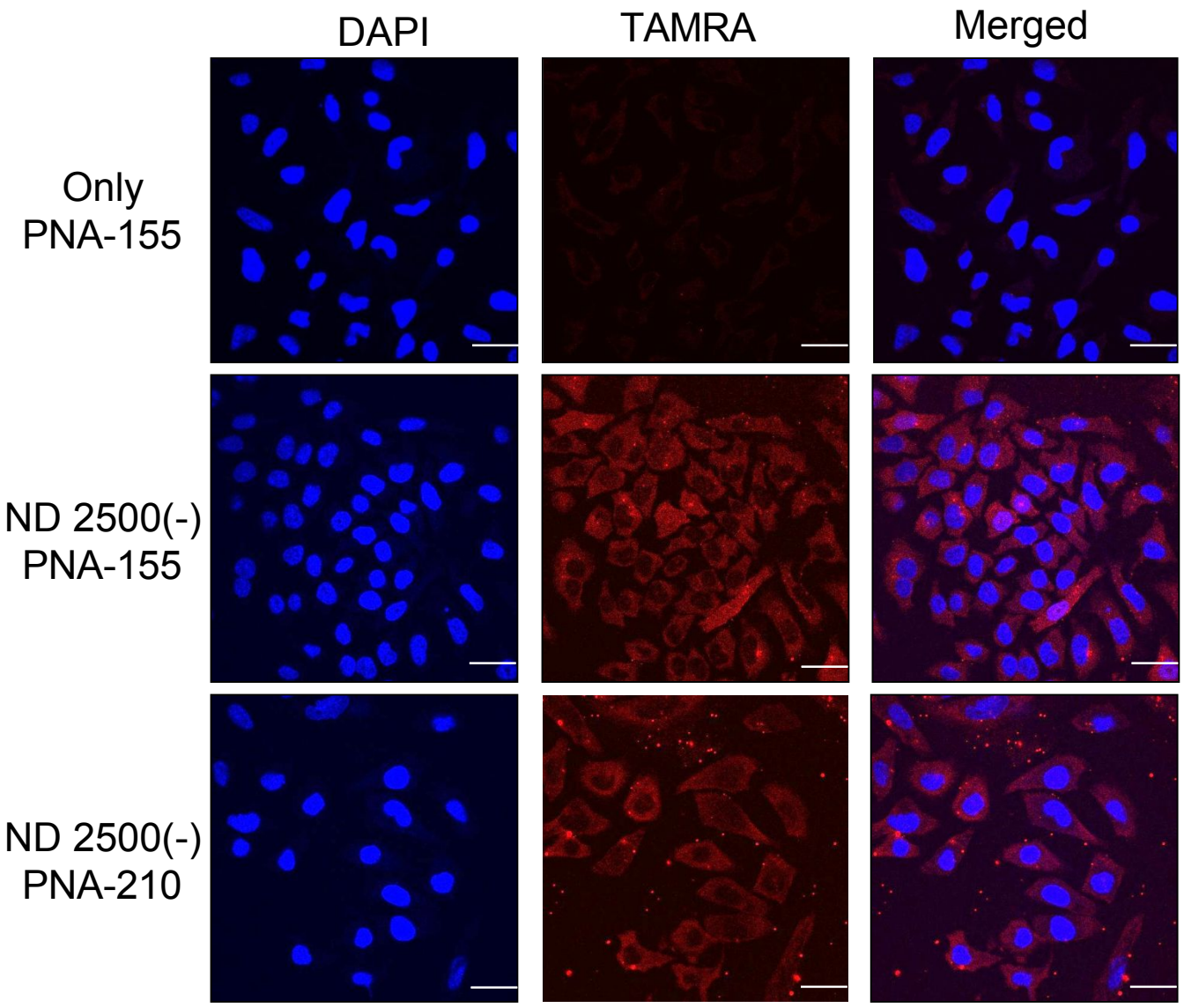

Fig 8

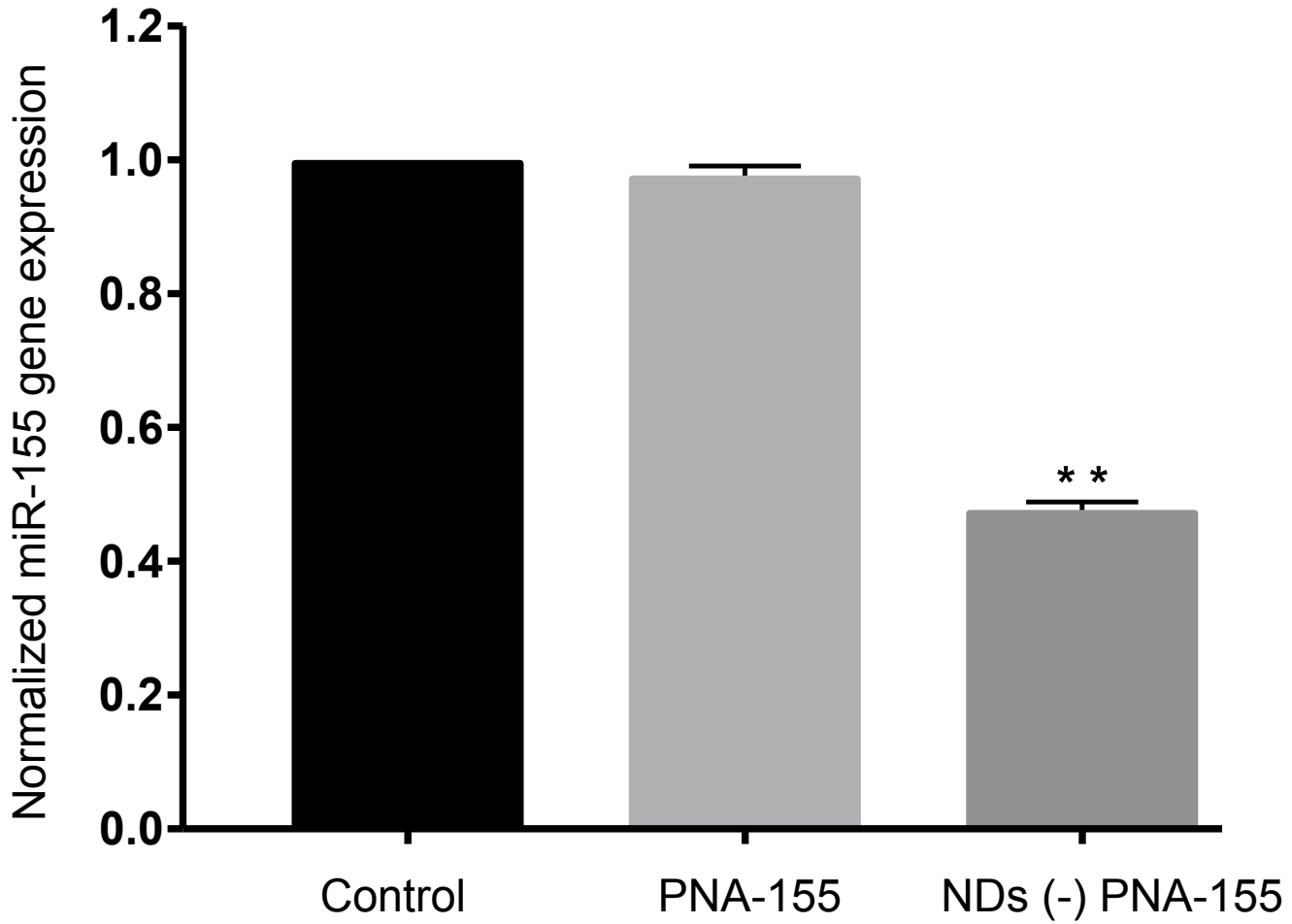
Normalized miR-155 gene expression
1.2
1.0
0.8
0.6
0.4
0.2
0.0
* *
Control
PNA-155
NDs (-) PNA-155

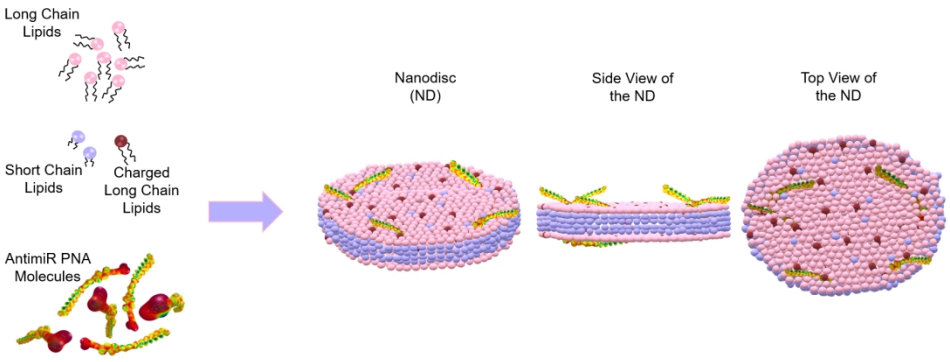

334x128mm (150 x 150 DPI)